# Experimental evidence that viscous shear zones generate periodic pore sheets that focus mass transport

James Gilgannon[1], Marius Waldvogel[1], Thomas Poulet[2], Florian Fusseis[3], Alfons Berger[1], Auke Barnhoorn[4], and Marco Herwegh[1]

[1]Institute of Geological Sciences, University of Bern, 3012 Bern, Switzerland
[2]CSIRO Mineral Resources, Kensington, WA 6151, Australia
[3]School of Geosciences, The University of Edinburgh, Edinburgh EH9 3JW, UK
[4]Department of Geoscience and Engineering, Delft University of Technology, Delft, The Netherlands

**Correspondence:** James Gilgannon (james.gilgannon@geo.unibe.ch)

**Abstract.** In experiments designed to understand deep shear zones, we show that periodic porous sheets emerge spontaneously during viscous creep, forming a hydro-mechanical anisotropy that influences mass transfer. These findings challenge the current paradigm of viscosity in solid rocks. In particular, they showcase how shear zones may actively focus mass transport and highlight the possibility that viscous rocks could locally transition from flow to fracture. Our work demonstrates that viscosity
5 in solids is not directly comparable to viscosity in fluids and this is consequential for a range of important solid Earth topics, like slow earthquakes, the flow of glacial ice and the tectonics of exoplanets.

## 1   Introduction

Our existing models for mantle convection, the advance of glaciers and even the dynamics of the seismic cycle all include, and rely on, the concept that solids can be viscous and flow with time. In this sense, the fluid mechanical concept of viscosity is
10 a cornerstone of Geoscience and our view of a dynamic Earth is built around it. In rocks, a record of this viscosity is found in mylonitic shear zones, the largest of which are the deep boundaries of tectonic plates that can reach into the asthenospheric upper mantle (Vauchez et al., 2012). Consequentially, mylonites represent important interfaces in the lithosphere that cross-cut different geochemical, geophysical and hydrological domains. This role places them at the centre of discussions on slow earthquakes and the hydrochemical exchange of deep and shallow reservoirs. In this context, it is critical to have a robust and
15 complete model of deep shear zones and the viscous rocks in them.

The accepted conceptual model for lithospheric shear zones supposes that there is a mechanical stratification with depth from an upper frictional to lower viscous domain (Sibson, 1977; Schmid and Handy, 1991; Handy et al., 2007). In this model, viscous deformation is a continuous slow background deformation and, at certain conditions, is punctuated by fracturing. It
20 is this episodic fracturing, driven by non-isochoric chemical reactions or frictional embrittlement, that creates seismicity and mass transport pathways through the deep Earth (Sibson, 1994). Two core assumptions of this conceptual model are that viscous creep mainly contributes to distorting the rock mass (Kocks et al., 1975) and the large confining pressures of the viscous

domain reduce porosity and permeability with compaction (Edmond and Paterson, 1972; Xiao et al., 2006). In contrast, there
is a newer paradigm which argues that viscous creep can intrinsically produce a dynamic permeability, called creep cavitation
25   (Fusseis et al., 2009). The presence of such a permeability would fundamentally change the role of viscous rocks during litho-
spheric deformation.

The proposed dynamic permeability is created and sustained by the opening and closure of syn-kinematic pores, called
creep cavities, during creep. In polymineralic viscous shear zones, the formation of creep cavities is postulated to establish an
30   advective mass transport pump (Fusseis et al., 2009; Menegon et al., 2015; Précigout et al., 2019), aid melt migration (Závada
et al., 2007) and has even been speculated to nucleate earthquakes (Shigematsu et al., 2004; Dimanov et al., 2007; Rybacki
et al., 2008; Verberne et al., 2017). Currently, much of the evidence supporting this new paradigm is limited to deformation
experiments on fabricated geo-materials and is generally restricted to grain-scale observations. Hence it has been difficult to
evaluate if this phenomenon is extensive and relevant in natural shear zones. In this contribution we provide unambiguous
35   experimental evidence in a natural starting material that supports, and extends, the paradigm concerning the role of creep
cavities in shear zones. We present quantitative results showing that creep cavities are a spatially significant feature of viscous
deformation. We argue that our results warrant a reappraisal of viscous creep to include creep cavitation into the general viscous
shear zone model.

## 2   New results from classical experiments

40   To make this argument, we have revisited a set of classical shear zone formation experiments preformed on Carrara marble
(Barnhoorn et al., 2004). The torsion experiments were run at a high homologous temperature (T = 1000 K, $T_h$ = 0.6) with
confining pressure (P = 300 MPa) at constant twist rates. Samples were deformed to large shear strains and recorded the dy-
namic transformation of undeformed, homogeneous, coarse-grained marbles into fine-grained ultramylonites. The experiments
demonstrated that microstructural change by dynamic recrystallisation was concurrent with mechanical weakening and the de-
45   velopment of a strong crystallographic preferred orientation. More recently, it was shown that these experiments contain creep
cavities and that the pores emerged with, and because of, grain-size reduction by sub-grain rotation recrystallisation (Gilgannon
et al., 2020). In this contribution we expand on these observations and present new results that quantify and contextualise the
development of porosity inside of an evolving viscous shear zone.

### 2.1   Porosity evolution with mylonitisation

50   At very low shear strains, and before any dynamic recrystallisation, pores decorate grain boundaries and appear as trails through
large grains (d ≈ 200 $\mu$m, fig. 1a). These pores are likely fluid inclusions trapped in and around the original grains (Covey-
crump, 1997) (the porosity density map in fig. 1b reflects this by highlighting the outlines of the initial grain-size). In the
experiment run to a shear strain of 5, which is in the midst of significant microstructural adjustment, the porosity has a clearly
different character. The pores appear at the triple junctions of small recrystallised grains (d ≈ 10 $\mu$m) and in some case are
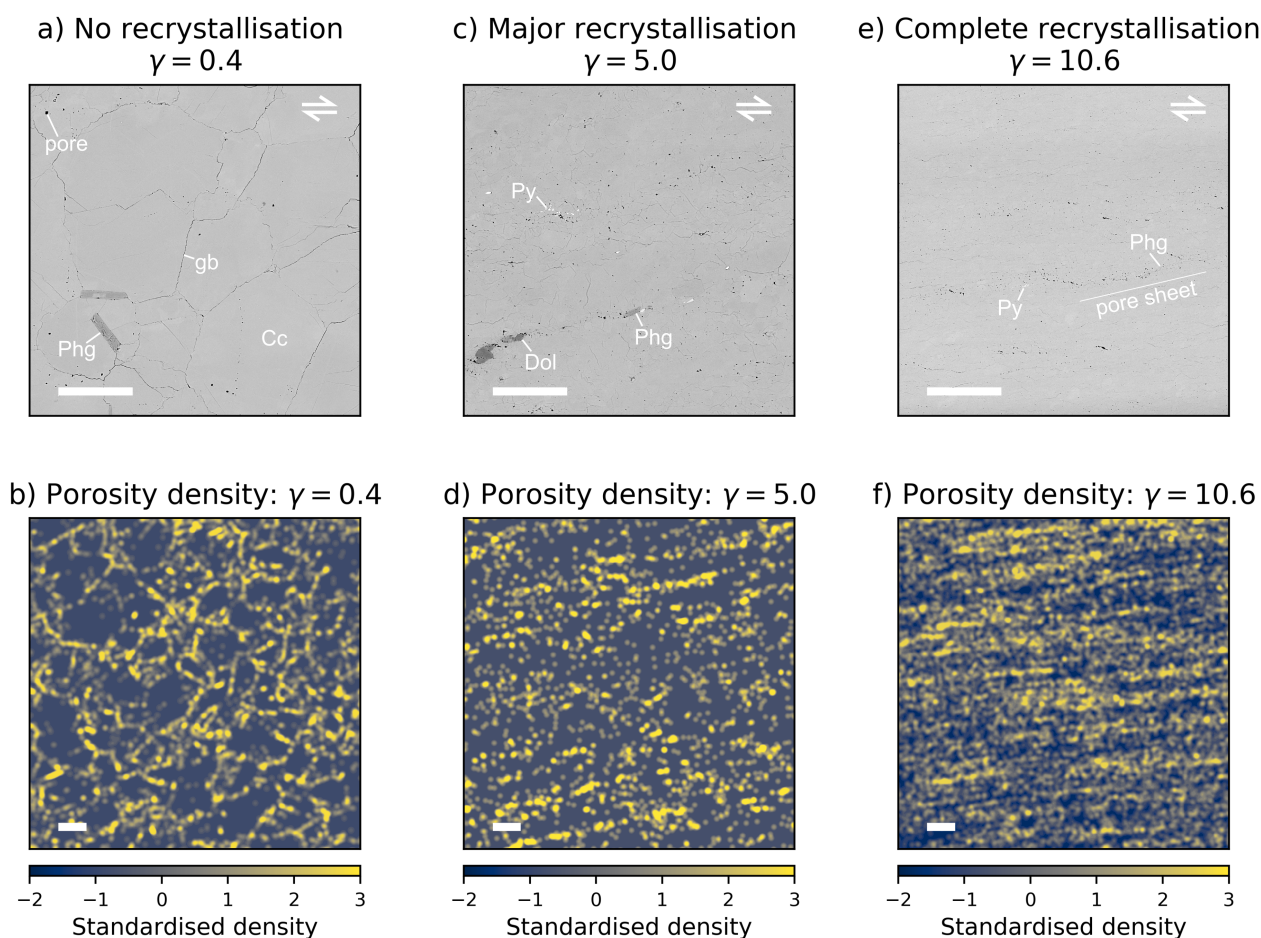
**Figure 1.** Microstructure and porosity density in samples with increasing strain. The samples document the production of a mylonite through dynamic recrystallisation. In all images the white scale bar is 100 $\mu m$. (Py = pyrite, Dol = dolomite, Phg = phengite, Cc = calcite, gb = grain boundary).

55    filled with new precipitates (fig. 1c). The porosity density map of this experiment highlights that pores appear in clusters that repeat across a large area and are systematically oriented (fig. 1d). Once the microstructure is fully recrystallised ($\gamma = 10.6$), and has reached a microstructural steady state, the porosity forms elongated sheets which also contain new precipitates of phengite and pyrite (fig. 1e). The density map of this experiment reveals that this porosity has become more spatially extensive and also shows a systematic orientation (fig. 1f). The implication of newly precipitated minerals is that the sheets are permeable and act
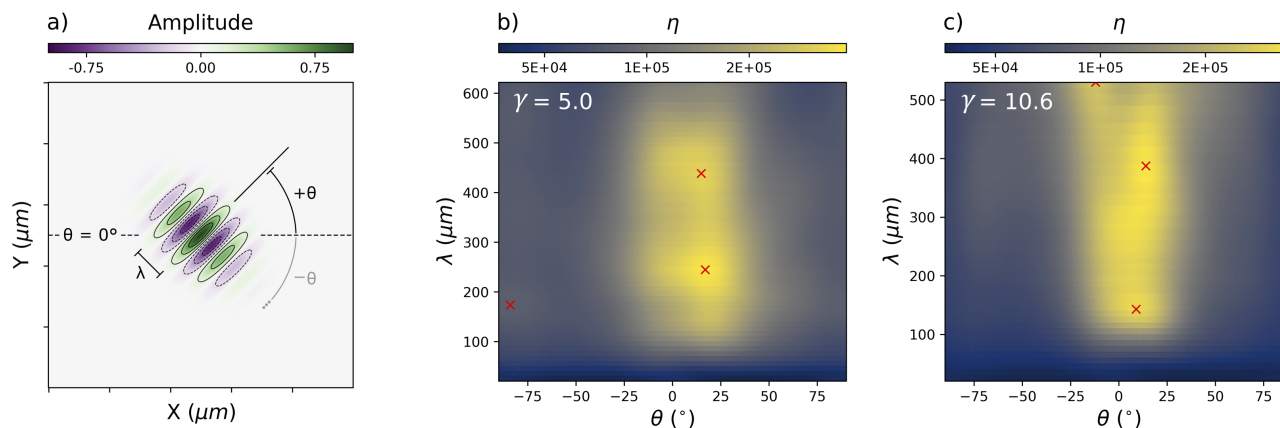
60    as mass transfer pathways.

**Figure 2.** Wavelet analysis of partly ($\gamma = 5.0$) and fully ($\gamma = 10.6$) recrystallised samples. Fig 2a show's a generic 2D Morlet wavelet. The wavelet analysis is conducted by considering the wavelet's interaction with the porosity density maps at each spatial position. This is repeated for different orientations ($\theta$) and wavelengths ($\lambda$). Figures 2b and c visualises the wavelet analysis results for the two samples. Peaks in $\eta$ represent the largest interaction with the wavelet. Peaks are identified by local extremes in $\eta$ and marked with red crosses.

## 2.2    2D continuous wavelet analysis of pore sheets

We quantify the spatial extent and character of these permeable pore sheets with 2D continuous wavelet analysis. In particular, we use the fully-anisotropic 2D Morlet wavelet (Neupauer and Powell, 2005) to identify features in the pore density maps and expand a 1D scheme of feature significance testing used in climate sciences (Torrence and Compo, 1998) to 2D to filter for

65    noise in the data. Furthermore, by implementing a 2D (pseudo) cone of influence we exclude boundary effects of the analysis at large wavelengths. For details of the wavelet analysis see the Methods section. Fundamentally, wavelet analysis can be thought of as a filter that highlights where the analysed data interacts with the wavelet most strongly. By varying the size and orientation ($\lambda$ and $\theta$ in fig 2a) of the Morlet wavelet one can isolate significant features in the data and gain quantitative information about them, including orientation, dimension and any spatial frequency.

70

Wavelet analysis reveals that, in both the partly and fully recrystallised samples, porosity is highly ordered with a strong periodicity and anisotropy. Both samples show two dominant modes of porosity distribution (fig. 2b and c). While the sample is only partly recrystallised, porosity is preferentially oriented at 17 and 15 degrees (measured antithetically in relation to the shear plane, see fig. 2a) with wavelengths of 245 and 438 $\mu$m respectively (fig. 2b and fig. 3a, b and c). This is both contrasted

75    and complemented by the modes found in the fully recrystallised experiment, where the anisotropy is oriented at 9 and 14 degrees with wavelengths of 143 and 387 $\mu$m, respectively (fig. 2c and fig. 3d, e and f). Interestingly the longer wavelength porosity features in both samples share similar orientations and spacing ($\Delta$ 1°, $\Delta$ 50 $\mu$m). As wavelet analysis does not require
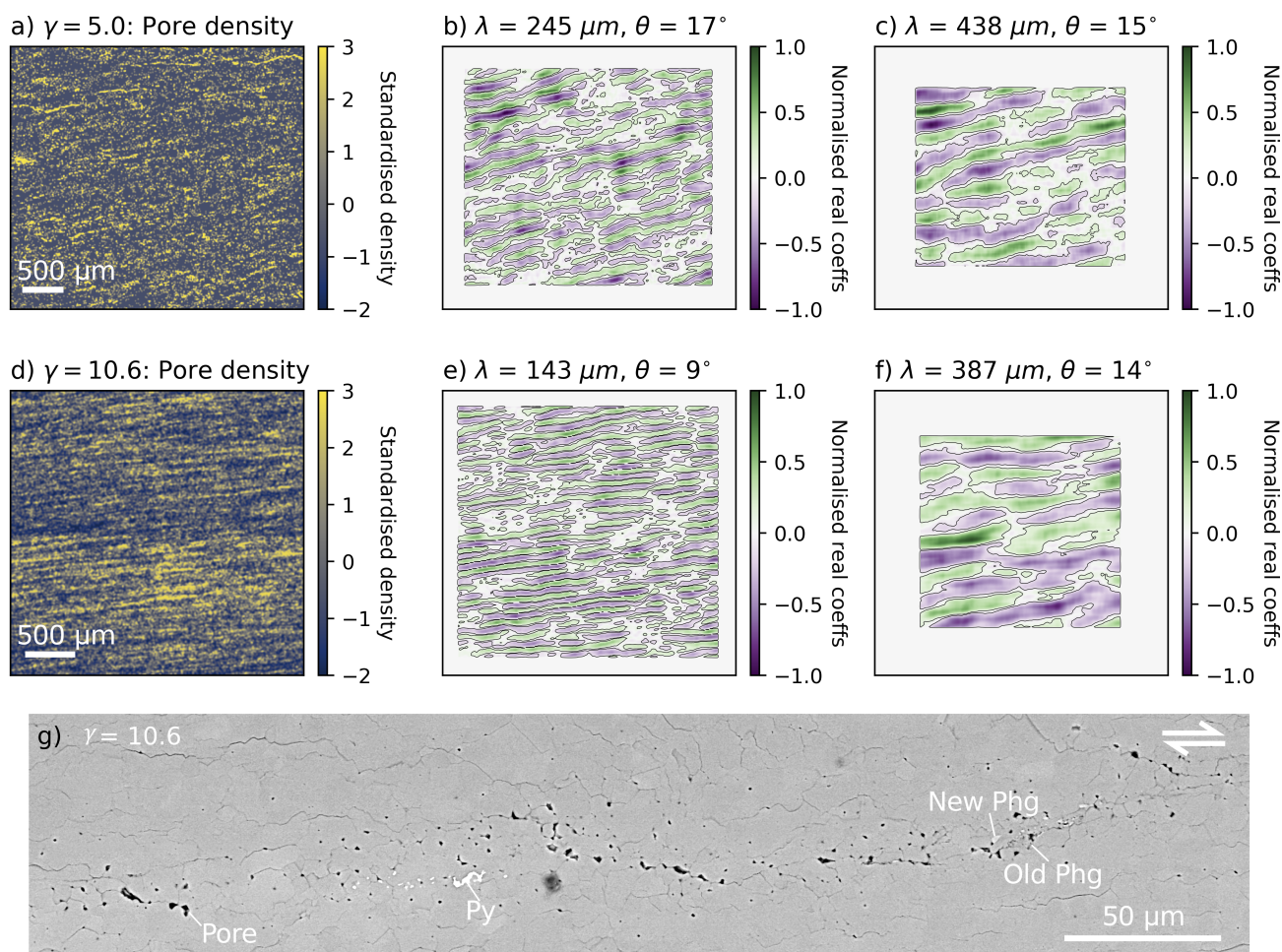
**Figure 3.** Visualisation of where the wavelet analysis identified anisotropy in the partly (figs 3a-c) and fully (figs 3d-f) recrystallised samples. For both samples the visualisation shows the wavelengths and orientations identified by peaks in figure 2. Figure 3g presents a more detailed view of the pore sheet labelled in figure 1e. (Phg = phengite).

features to be periodic to be identified, the periodicity is a result and not an artefact of the analysis. Figure 3g showcases, in more detail, an example of the pore sheets identified by the wavelet analysis.

## 3 Discussion

These results provide an unambiguous foundation for discussing the community's model of viscosity in solids at high homologous temperatures. Chiefly, our results show that viscous shear zones spontaneously develop highly anisotropic periodic porous

sheets. Currently, this is not accounted for in our conceptual models and should be integrated as it has important consequences for deformation in nature.

### 3.1 How mylonites focus mass transport

85

Firstly, we suggest that the presence of periodic, porous sheets in natural shear zones would act to focus fluid during active deformation. Geochemical studies have proposed that the enrichment or depletion of elements in purely viscous shear zones must reflect syn-deformational fluid migration (e.g. Carter and Dworkin, 1990; Selverstone et al., 1991). Our results provide an experimental insight into the microstructure of the syn-kinematic pore network that likely facilitates this fluid transport.

90 Furthermore, this validates the prediction of pore sheets in the dynamic granular fluid pump model (Fusseis et al., 2009) and extends it to show that pore sheets can develop spontaneously in homogenous rocks, with a periodic and oriented character. Curiously, our results also seem to suggest that porous domains develop within zones of stable orientation and, possibly, wavelength (approx. 15° from the shear zone boundary with a wavelength of 400 $\mu m$). This is consequential because it implies that the emergence of porous sheets is determined by bulk material properties and not by any initial heterogeneity in the

95 material. A question that naturally arises from this is, how would periodic porous sheets affect the mechanical behaviour of the deep lithosphere?

### 3.2 A spontaneous change from flow to fracture

We argue that the appearance of pore sheets during deformation could allow for the mechanical behaviour of a viscous shear zone to spontaneously change from flow to fracture. This change can never be predicted by flow laws commonly used to

100 model viscous deformation in the lithosphere and, if correct, our interpretation challenges the sole use of such flow laws in these applications. Two earlier examples of this problem were documented in large strain deformation experiments on synthetic gabbros and synthetic anorthite aggregates (Dimanov et al., 2007; Rybacki et al., 2008). In those experiments, creep fractures were shown to evolve out of deformation characterised by strain invariant mechanical parameters for linear viscous flow. Our experiments were also found to have constant mechanical parameters with strain (Barnhoorn et al., 2004), and we

105 speculate that the pore sheets we observe could evolve into creep fractures in a natural setting. We suggest this because natural conditions are more varied, both in magnitude and in time, than those tested by our experiments. In this natural setting a fluid-filled pore sheet may become mechanically unstable and collapse during deformation. This process may even cascade and the instability of one sheet may propagate to others, which may explain how both ambient and teleseismically triggered tremors can occur at depths below the seismogenic zone (Wang and Tréhu, 2016). This interpretation places pore sheets, alongside

110 brittle fracturing and non-isochoric chemical reactions, as the potential nuclei of slow earthquake phenomena. Furthermore, as the emergence of creep cavities was linked to dynamic recrystallisation (Gilgannon et al., 2020), a process expected throughout the lithosphere, the hydro-mechanical anisotropy presented here would allow slow earthquake phenomena to occur across a range of metamorphic conditions and mineralogical compositions (Peacock, 2009).

## 4  Conclusions

115  In summary, the current paradigm of viscosity that is borrowed from fluids is not a completely adequate analogy for solid geomaterials. We have shown that as rocks deform viscously, they spontaneously develop a hydro-mechanical anisotropy. This would not be expected within the current paradigm. On this basis, we advocate for an update to the current concept of viscosity at high temperatures and pressures in rocks to include the viscous hydro-mechanical anisotropy we have presented. Our discussion has explored some of the possible consequences of changing our paradigm and moving forward these speculations

120  should be integrated and tested. As the viscosity of solids is a cornerstone of Geoscience, our results have farther reaching implications than the conceptual shear zone model and may even be relevant for other scenarios where solid state deformation is modelled with viscous rheologies, like glacial flow (e.g. Egholm et al., 2011) and tectonics on exoplantes (e.g. Noack and Breuer, 2014).

*Code and data availability.*  Available from James Gilgannon.

125  **Appendix A: Methods**

The results of the main manuscript come from the investigation of 3 experimental samples (see table A1). Each sample was imaged using scanning electron microscopy, segmented and analysed. In the following the data acquisition, processing and analysis used will be outlined. For a description of the starting material or the original experimental procedure please refer to Barnhoorn et al. (2004) and Gilgannon et al. (2020).

130  **A1  Acquisition of large backscatter electron mosaics**

Three large BSE maps were acquired on a Zeiss Evo 50 SEM with a QBSD semiconductor electron detector (acceleration voltage = 15 kV; beam current $\approx$ 500 pA). In each case the maps were stitched together by the Zeiss software Multiscan. The pixel dimensions and scales are listed in table A2.

**Table A1.** Experimental samples revisited

| Sample | $\dot{\gamma}$ | $\gamma_{max}$ | Amount of recrystallisation |
|--------|--------|--------|-----------------------------|
| PO344 | $3 \times 10^{-4}$ | 0.4 | None |
| PO422 | $3 \times 10^{-4}$ | 5.0 | Major[a] |
| PO265 | $2 \times 10^{-3}$ | 10.6 | Complete[b] |

[a] 65-90 % as classified by Barnhoorn et al. (2004)

[b] 90-100 % as classified by Barnhoorn et al. (2004)

Solid Earth
Discussions

Open Access

EGU

**Table A2.** Dimensions and resolutions of mosaics

| Sample | $\gamma_{max}$ | Pixel dimensions | Scale (px : $\mu m$) |
|--------|------|------------------|---------------------|
| PO344  | 0.4  | 15000 x 13944    | 1 : 0.36            |
| PO422  | 5.0  | 8745 x 7392      | 1 : 0.55            |
| PO265  | 10.6 | 21127 x 20494    | 1 : 0.16            |

## A2   Segmentation for porosity

We used the segmentation, labelling and filtering work flow described in Gilgannon et al. (2020). In this work flow grain boundaries must be filtered for by using each labelled feature's aspect ratio. Specifically, the data is filtered to remove features with aspect ratios greater than 4. Figure S1 shows all features initially labelled as porosity by the segmentation process in each sample. These are plotted for their area and perimeter, while colour coded for aspect ratio. In each data set there are two trends:

1. Features with aspect ratios $> 4$ that show area-perimeter relationships for lines of widths between 0.25-1.25 $\mu m$

2. Features with aspect ratios $< 4$ that do not show area-perimeter relations of a line

Based on this criteria, only features with aspect ratios of $< 4$ are considered as pores. The centroids of features meeting this criteria were then extracted and used in the kernel point density analysis.

## A3   Kernel density estimator maps

At the first instance, one of the major difficulties in understanding the relationship of micron scale features across millimetres is simply visualising the problem. We utilised the kernel density (KDE) for point features function in ESRI's ArcGIS v10.1 software to overcome this issue. This has the effect of converting point data, that only tell us something about individual pores, to a map that considers the distribution of pores and, in part, their relation in space.

We manually set the output cell size and search radius to 1 $\mu m$ and 20 $\mu m$, respectively. The kernel smoothing factor was automatically calculated with reference to the population size and the extent of analysis and contoured based on a 1/4 $\sigma$ kernel. We specifically did not use the default search radius (calculated with Silverman's Rule of Thumb). Our intention here was to retain as much data as possible in the visualisation. In this way we visualised local neighbourhoods and produced an image for further analysis that had not been overly smoothed. It was these density maps that we then quantitatively analysed with 2D continuous wavelet analysis.

## A4   2D Continuous wavelet analysis

Wavelets are highly localised waveforms that can be used to analyse signals with rising and falling intensity. Our images are such signals. Simply put, wavelets can be used to reveal the location (in space or time) and the frequency at which the most
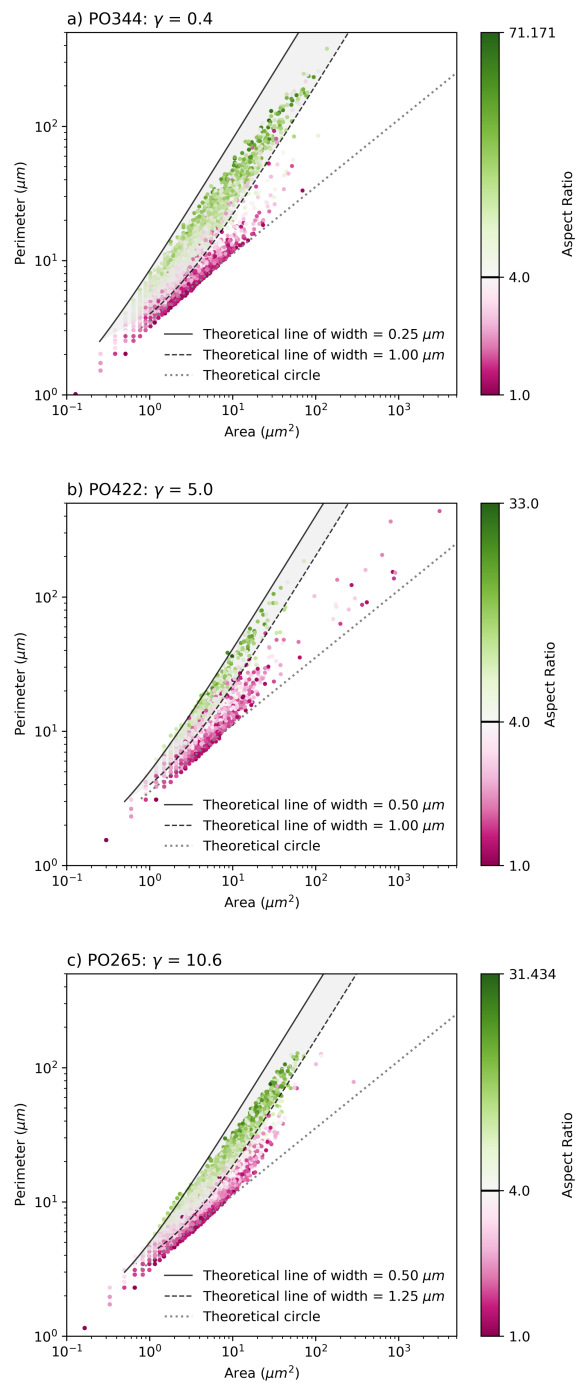
**Figure A1.** Filtering criteria for grain boundaries and pores.

significant parts of a signal can be found. Continuous wavelet analysis is the particular wavelet-based method that we employ in this contribution.

160

To identify features at different frequencies the wavelet is stretched over what are knows as different scales ($a$). The scales relate to the central frequency of the wavelet, which in turn can be related to the wavelength ($\lambda$):

$$\lambda = \frac{4\pi a}{k_0 + \sqrt{k_0^2 + 4}} \tag{A1}$$

where $k_0$ is the wavenumber.

165

In the broadest sense, a wavelet can be seen as a filter that finds peaks in an image. To do this it is shifted around the spatial domain ($\mathbf{x}$) of an image, by way of the shift parameter ($\mathbf{b}$), and this is repeated at different scales to find peaks. In this way features of different sizes can be located in space and in scale: short wavelengths highlight small features and long wavelengths larger ones. In this contribution, we utilise the fully anisotropic Morlet wavelet (Neupauer and Powell, 2005) because it also

170 allows features of varying orientation to be identified. The wavelet is considered to be fully anisotropic because it produces in-phase elongation along the wave vector, such that the wavelet can be rotated and maintain its anisotropy. The wavelet takes the form:

$$\mathbf{\Psi}(\mathbf{x}, \theta, L) = e^{i\mathbf{k}_0 \cdot \mathbf{Cx}} \, e^{-1/2(\mathbf{Cx} \cdot \mathbf{A}^T \mathbf{A} \mathbf{Cx})} \tag{A2}$$

Where $\theta$, $L$, $\mathbf{k}_0$, $\mathbf{C}$ and $\mathbf{A}$ are the angle for the rotation matrix, ratio of anisotropy, wave vector, rotation matrix and anisotropy

175 matrix, respectively. The non-scalar terms are given by:

$$\mathbf{k}_0 = (0, k_0), \, k_0 > 5.5 \tag{A3}$$

In this study we use $k_0 = 6.0$.

$$\mathbf{C} = \begin{bmatrix} cos\,\theta & -sin\,\theta \\ sin\,\theta & cos\,\theta \end{bmatrix} \tag{A4}$$

This rotation matrix rotates the entire wavelet by $\theta$, which is defined as positive in a counter-clockwise direction with respect

180 to the positive x axis (see fig. 2 of the main manuscript).

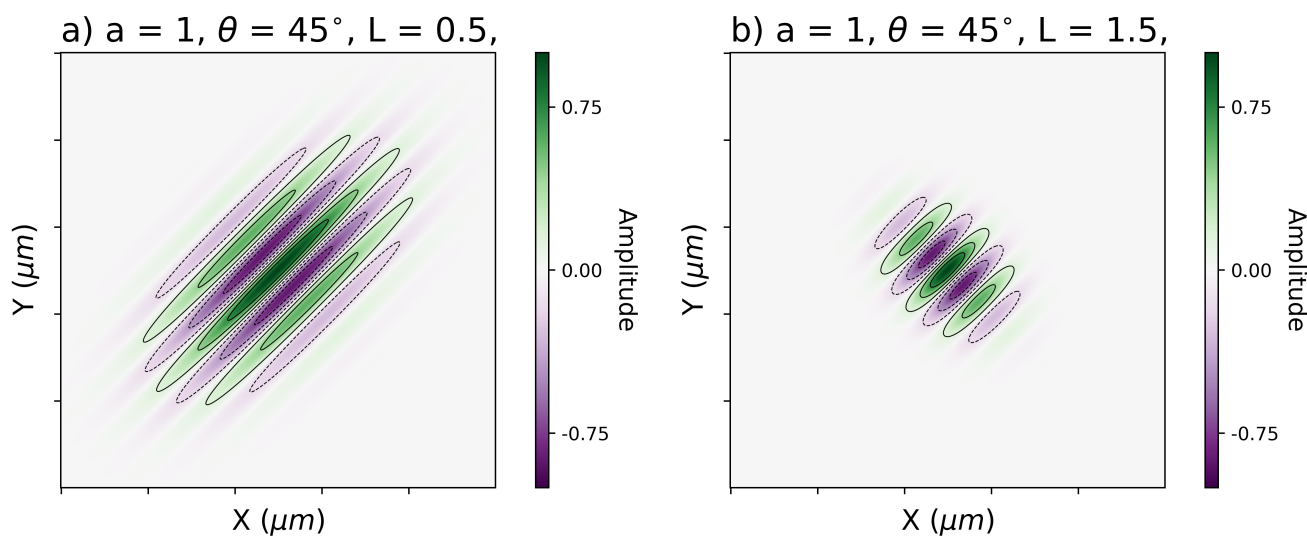$$\mathbf{A} = \begin{bmatrix} L & 0 \\ 0 & 1 \end{bmatrix} \tag{A5}$$

**Figure A2.** Examples of how a wavelet changes with the anisotropy ratio (L).

Where the ratio of anisotropy ($L$) is defined as the ratio of the length of the wavelet perpendicular to $\theta$ over the length parallel to $\theta$. In this way, values of $L < 1$ represent extreme anisotropy parallel to the angle of the wavelet.

185    We chose to use an anisotropy ratio of $L = 1.5$ (see fig. S2). This was done because the input images are kernel density maps and the estimator used is circular. We wanted our wavelet to utilise its inherent anisotropy and angular selectivity to identify extended concentrations of the estimator that would appear as elliptical clusters of circles. We did not use an $L < 1$ as these wavelets anisotropies are too far from the shapes expected from the features we investigated (Torrence and Compo, 1998). If, for example, we had been investigating linear features like fractures we would have used a more anisotropic wavelet shape (for

190    example, $L = 0.5$).

To ensure that the total energy of the analysing wavelet is independent of the scale of analysis the relationship between the wavelet (eq.A2) and the mother wavelet is:

$$\mathbf{\Psi}_{a,\mathbf{b}}(\mathbf{x}, \theta, L) = \frac{\sqrt{L}}{a} \mathbf{\Psi}\left(\frac{\mathbf{x} - \mathbf{b}}{a}, \theta, L\right) \tag{A6}$$

195    To be clear, we refer, above, to energy in the generalized sense of signal processing.

Our input images for wavelet analysis are 8-bit kernel density maps of pore centroids. Each density map can be considered as an intensity function ($\mathbf{I}(\mathbf{x})$) who's magnitude limits are 0 and 255. We standardise each input image such that,

$$\mathbf{I}_{std}(\mathbf{x}) = \frac{\mathbf{I} - \mu}{\sigma} \tag{A7}$$

200    Where $\mu$ and $\sigma$ are the image's mean and standard deviation. This is because the best results of wavelet analysis are achieved on a zero-mean random field (Neupauer and Powell, 2005).

It is on this new standardised image that we preform the wavelet transformation. The wavelet transformation of $\mathbf{I}_{std}(\mathbf{x})$ is a convolution with the analysing wavelet:

205    $$\mathbf{W}_{\mathbf{\Psi}} f(\mathbf{b}, a, \theta, L) = \frac{\sqrt{L}}{a} \int\limits_{-\infty}^{\infty} f(\mathbf{x}) \bar{\mathbf{\Psi}} \left( \frac{\mathbf{x} - \mathbf{b}}{a}, \theta, L \right) d\mathbf{x} = \frac{\sqrt{L}}{a} f(\mathbf{b}) * \bar{\mathbf{\Psi}} \left( -\frac{\mathbf{b}}{a}, \theta, L \right) \tag{A8}$$

Here, $*$ is the convolution and the overbar denotes the complex conjugate. The convolution is evaluated by taking the inverse fast Fourier transform of the products of the Fourier transforms of $f(\mathbf{b})$ and $\bar{\mathbf{\Psi}}(-\mathbf{b}/a, \theta, L)$. This wavelet and the convolution follow those outlined in Neupauer and Powell (2005).

## A5   Defining significance

210   As outlined above, wavelet analysis will highlight regions of an image where the wavelet and the image interact strongly. This interaction alone is not enough to say that what the wavelet highlighted is relevant when compared to any expected noise in the image. Therefore, it is important to know if the areas highlighted by the wavelet are significant. To define what is significant in the analysis we adopt the method outlined in Torrence and Compo (1998).

215    The general assumption of the null hypothesis is that the image analysed has some mean power spectrum ($P_k$, see equation 16 in Torrence and Compo (1998)), related to a background geophysical process(es). If the wavelet power spectra is found to be significantly above this background spectrum then the feature is *a real anomaly* and not a result of the assumed background process(es).

220    To test the null hypotheses, the local wavelet power spectrum at each scale (following equation 18 in Torrence and Compo (1998)) must be considered:

$$\frac{|W_{\mathbf{b}}(a)^2|}{\sigma^2} \implies \frac{1}{2} P_k \chi_2^2 \tag{A9}$$

Where $|W_{\mathbf{b}}(a)^2|$ is the local power, $\sigma^2$ is the variance, $\implies$ indicates 'is distributed as' and $\chi_2^2$ represents a chi-square distribution with two degrees of freedom. Using the relation in eq. A9 one can find how significantly the local wavelet power
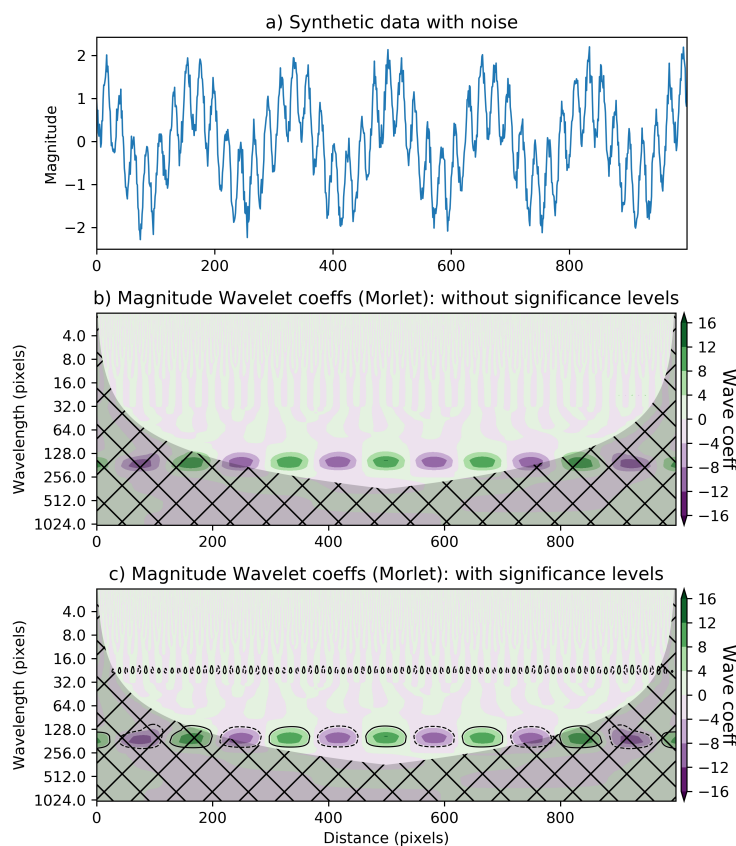
**Figure A3.** Example of why significance test is needed. a) is a 1D synthetic, noisy, signal made of 2 waves, of different wavelengths. b) and c) present the 1D wavelet transformation of (a) with a 1D Morlet wavelet: in (b) the result is only visualised, while in (c) the significance test is also visualised. In both, the hatched area contains edge effects and is delimited by a 1D cone of influence. The contouring in (c) shows domains that are within the 95% confidence level of not being white noise. The contours highlight values that are both positively and negatively larger than the white noise model. The takeaway message is that the significance test is needed to accurately identify regions of 'real anomaly'.

225    deviates from the background spectrum. To do this, the mean background spectrum, $P_k$ (where $k$ is the Fourier frequency), is multiplied by the 95th percentile value of $\chi_2^2$ to give a 95% confidence level. As the local wavelet power is distributed equivalently, this confidence level can be used to contour the global wavelet power ($|\mathbf{W_\Psi}^2|$). The result allows the identification of data that has a 95% chance of not being a random peak from the background spectrum (see fig. S3).

230      In this contribution we adopted a white noise model as our background spectra. White noise is a random signal that assumes a uniform power across frequencies. We chose this because we wish to identify when porosity density is non-random and, based on our knowledge of the active processes, we consider that any noise will be uniform across the scales of analysis. We

make this assumption about the background spectra for the following reasons.

235     The experiments we revisit are non-localising at the sample scale and are considered as the exemplar of a sub-solidus, homogenous, viscous deformation. The prevailing assumption for such a sample being deformed is that the microstructural change will first occur where locally favourable conditions allow. For example, some poorly oriented grains may develop more deformation induced defects and be prone to recrystallise earlier than other grains. The general distribution of grain orientations is determined by the starting material's texture, which in the case of Carrara marble is random (Pieri et al., 2001). Therefore,
240     as there is not any initial anisotropy in grain orientations, it is expected that porosity will form randomly in space at favourable sites in the microstructre. Any deviation from this expectation is of interest to us. For these reasons, we use a white noise model as our background spectra and it forms the reference for testing where the porosity density is non-random.

        As stated in the main text, it was shown for our experiments that creep cavities emerged with, and because of, grain size
245     reduction by sub-grain rotation recrystallisation *(18)*. The white noise null hypothesis used supposes that this grain size change and porosity development occurred with no preference in space or frequency. By using this as our null model we can show when the wavelet analysis produces interactions that are very unlikely to have occurred randomly, and highlights heterogeneity and anisotropy in the porosity density maps.

## A6    Defining limits of the analysis

250 As images have finite length and width the analysing wavelet will misinterpret these edges and produce erroneously positive results. To avoid this one may use padding but ultimately the problem will remain (Torrence and Compo, 1998). Instead, we have chosen to implement a 2D cone of influence (COI). Starting from the edge of the image, the COI defines a zone in which data will likely suffer from edge effects (see area outside of red contour in fig. S4b). The zone increases proportionally with the wavelet scales. We consider our 2D COI as a pseudo-COI because we simply project two 1D COIs across the 2D surface.
255 We use the e-folding time defined by Torrence and Compo (1998) for their 1D Morlet wavelet, which is $\sqrt{2a}$. For both the y and x axis of the input image we can calculate the appropriate length 1D COI. Each of these 1D COIs is calculated for the set of discrete scales (a) defined for the wavelet transformation. At each scale, the y and x axis COIs are projected to produce a contour that defines the 2D COI at each scale (see fig. S4b and c).

260     In this way, our COI does not account for the wavelet's shape and anisotropy. While this means our COI is not the correct mathematical solution for defining where edge effects end for this 2D wavelet, it is a best first attempt at defining a limit to the analysis. We then delete data that lies within the COI. Furthermore, we define a *sensible* limit to the largest relevant scale of analysis by only considering scales which have *edge-effect-free* windows that are greater than 30% of the original image size.
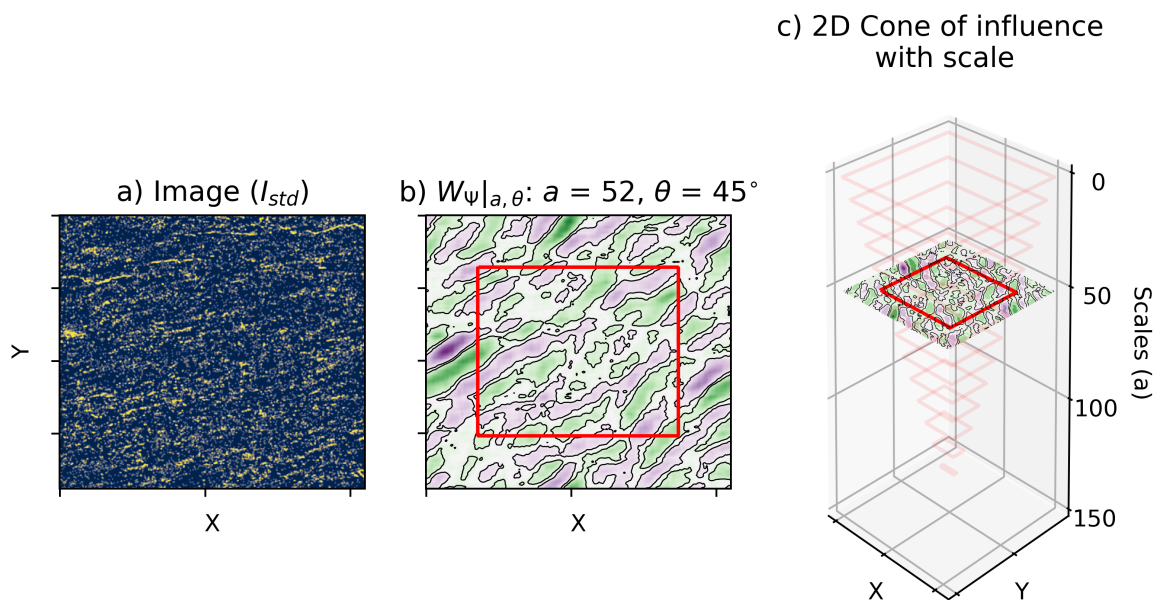
Solid Earth
Discussions

Open Access

EGU



**Figure A4.** Defining the limits of the analysis across scales. For some image (a), an arbitrary wavelet transformation is visualised at an arbitrary scale and angle (b). Here the black contours enclose data that is within the 95% confidence level. Overlaying this is a red contour which delimits the zone of possible edge effects of the analysis. At this scale this is a slice of the cone of influence (COI). c) visualises the COI across scales. As the scale, and therefore the wavelength of the analysing wavelet, increase, the zone without edge effects decreases. For the purposes of demonstration, data within the COI has not been removed in this figure.

## A7 Visualising wavelet results

265 Figure 2 of the main manuscript uses the global measure $\eta$ (Neupauer et al., 2006) to investigate peaks in the data. Here we define $\eta$ as:

$$\eta(a, \theta, L) = \int |W_\Psi^2| \, d\mathbf{b} \tag{A10}$$

As we use only one value of anisotropy, $\eta$ can be visualised to reveal information about peaks in orientation and scale. To quantitatively identify peaks in $\eta$ we use the *h_maxima* function (where h = 0.03) of the Scikit-image python library (van der
270 Walt et al., 2014).

*Competing interests.* There are no competing interests.

# References

Barnhoorn, A., Bystricky, M., Burlini, L., and Kunze, K.: The role of recrystallisation on the deformation behaviour of calcite rocks: large

280     strain torsion experiments on Carrara marble, Journal of Structural Geology, 26, 885–903, https://doi.org/10.1016/j.jsg.2003.11.024, 2004.

Carter, K. and Dworkin, S.: Channelized fluid flow through shear zones during fluid-enhanced dynamic recrystallization, Northern Apennines, Italy, Geology, 18, 720–723, https://doi.org/10.1130/0091-7613(1990)018<0720:CFFTSZ>2.3.CO;2, 1990.

Covey-crump, S.: The high temperature static recovery and recrystallization behaviour of cold-worked Carrara marble, Journal of Structural Geology, 19, 225–241, https://doi.org/10.1016/S0191-8141(96)00088-0, 1997.

285  Dimanov, A., Rybacki, E., Wirth, R., and Dresen, G.: Creep and strain-dependent microstructures of synthetic anorthite-diopside aggregates, Journal of Structural Geology, 29, 1049–1069, https://doi.org/10.1016/j.jsg.2007.02.010, 2007.

Edmond, J. and Paterson, M.: Volume changes during the deformation of rocks at high pressures, International Journal of Rock Mechanics and Mining Sciences & Geomechanics Abstracts, 9, 161–182, https://doi.org/10.1016/0148-9062(72)90019-8, 1972.

Egholm, D., Knudsen, M., Clark, C., and Lesemann, J.: Modeling the flow of glaciers in steep terrains: The integrated second-order shallow

290     ice approximation (iSOSIA), Journal of Geophysical Research: Earth Surface, 116, https://doi.org/10.1029/2010JF001900, 2011.

Fusseis, F., Regenauer-Lieb, K., Liu, J., Hough, R., and De Carlo, F.: Creep cavitation can establish a dynamic granular fluid pump in ductile shear zones, Nature, 459, 974–977, https://doi.org/10.1038/nature08051, 2009.

Gilgannon, J., Poulet, T., Berger, A., Barnhoorn, A., and Herwegh, M.: Dynamic recrystallisation can produce porosity in shear zones, Geophysical Research Letters, 47, e2019GL086 172, https://doi.org/10.1029/2019GL086172, 2020.

295  Handy, H., Hirth, G., and Bürgmann, R.: Continental Fault Structure and Rheology from the Frictional-to-Viscous Transition Downward, chap. 6, pp. 139–182, MIT Press, 2007.

Kocks, U., Argon, A., and Ashby, M.: Thermodynamics and kinetics of slip, vol. 19 of *Progress in Materials Science*, Pergamon Press Ltd, 1975.

Menegon, L., Fusseis, F., Stünitz, H., and Xiao, X.: Creep cavitation bands control porosity and fluid flow in lower crustal shear zones,

300     Geology, 43, 227–230, https://doi.org/10.1130/G36307.1, 2015.

Neupauer, R. and Powell, K.: A fully-anisotropic Morlet wavelet to identify dominant orientations in a porous medium, Computers & Geosciences, 31, 465–471, https://doi.org/10.1016/j.cageo.2004.10.014, 2005.

Neupauer, R., Powell, K., Qi, X., Lee, D., and Villhauer, D.: Characterization of permeability anisotropy using wavelet analysis, Water Resources Research, 42, https://doi.org/10.1029/2005WR004364, 2006.

305  Noack, L. and Breuer, D.: Plate tectonics on rocky exoplanets: Influence of initial conditions and mantle rheology, Planetary and Space Science, 98, 41–49, https://doi.org/10.1016/j.pss.2013.06.020, 2014.

Peacock, S.: Thermal and metamorphic environment of subduction zone episodic tremor and slip, Journal of Geophysical Research: Solid Earth, 114, https://doi.org/10.1029/2008JB005978, 2009.

Pieri, M., Kunze, K., Burlini, L., Stretton, I., Olgaard, D., Burg, J.-P., and Wenk, H.-R.: Texture development of calcite by deforma-

310     tion and dynamic recrystallization at 1000K during torsion experiments of marble to large strains, Tectonophysics, 330, 119–140, https://doi.org/10.1016/S0040-1951(00)00225-0, 2001.

Précigout, J., Stünitz, H., and Villeneuve, J.: Excess water storage induced by viscous strain localization during high-pressure shear experiment, Scientific Reports, 9, 3463, https://doi.org/10.1038/s41598-019-40020-y, 2019.

Rybacki, E., Wirth, R., and Dresen, G.: High-strain creep of feldspar rocks: Implications for cavitation and ductile failure in the lower crust,
315    Geophysical Research Letters, 35, https://doi.org/10.1029/2007GL032478, 2008.

Schmid, S. and Handy, M.: Towards a genetic classification of fault rocks - geological usage and tectonophysical implications, chap. 16, pp.
    339–361, Academic Press, New York, 1991.

Selverstone, J., Morteani, G., and Staude, J.-M.: Fluid channelling during ductile shearing: transformation of granodiorite into alu-
    minous schist in the Tauern Window, Eastern Alps, Journal of Metamorphic Geology, 9, 419–431, https://doi.org/10.1111/j.1525-
320    1314.1991.tb00536.x, 1991.

Shigematsu, N., Fujimoto, K., Ohtani, T., and Goto, K.: Ductile fracture of fine-grained plagioclase in the brittle-plastic
    transition regime: implication for earthquake source nucleation, Earth and Planetary Science Letters, 222, 1007–1022,
    https://doi.org/10.1016/j.epsl.2004.04.001, 2004.

Sibson, R.: Fault rocks and fault mechanisms, Journal of the Geological Society, 133, 191–213, https://doi.org/10.1144/gsjgs.133.3.0191,
325    1977.

Sibson, R.: Crustal stress, faulting and fluid flow, Geological Society, London, Special Publications, 78, 69–84,
    https://doi.org/10.1144/GSL.SP.1994.078.01.07, 1994.

Torrence, C. and Compo, G.: A Practical Guide to Wavelet Analysis, Bulletin of the American Meteorological Society, 79, 61–78,
    https://doi.org/10.1175/1520-0477(1998)079<0061:APGTWA>2.0.CO;2, 1998.

330   van der Walt, S., Schönberger, J., Nunez-Iglesias, J., Boulogne, F., Warner, J., Yager, N., Gouillart, E., Yu, T., and the scikit-image contrib-
    utors: scikit-image: image processing in Python, PeerJ, 2, e453, https://doi.org/10.7717/peerj.453, 2014.

Vauchez, A., Tommasi, A., and Mainprice, D.: Faults (shear zones) in the Earth's mantle, Tectonophysics, 558-559, 1–27,
    https://doi.org/10.1016/j.tecto.2012.06.006, 2012.

Verberne, B., Chen, J., Niemeijer, A., de Bresser, J., Pennock, G., Drury, M., and Spiers, C.: Microscale cavitation as a mechanism for
335    nucleating earthquakes at the base of the seismogenic zone, Nature Communications, 8, 1645, https://doi.org/10.1038/s41467-017-01843-
    3, 2017.

Wang, K. and Tréhu, A.: Invited review paper: Some outstanding issues in the study of great megathrust earthquakes - The Cascadia example,
    Journal of Geodynamics, 98, 1–18, https://doi.org/10.1016/j.jog.2016.03.010, 2016.

Xiao, X., Evans, B., and Bernabé, Y.: Permeability Evolution During Non-linear Viscous Creep of Calcite Rocks, pp. 2071–2102, Birkhäuser
340    Basel, Basel, https://doi.org/10.1007/978-3-7643-8124-0_3, 2006.

Závada, P., Schulmann, K., Konopásek, J., Stanislav, U., and Ondrej, L.: Extreme ductility of feldspar aggregates - Melt-enhanced grain
    boundary sliding and creep failure: Rheological implications for felsic lower crust, Journal of Geophysical Research: Solid Earth, 112,
    https://doi.org/10.1029/2006JB004820, 2007.